Simplified spherical harmonic method for coupled electron-photon transport calculations

J. A. Josef and J. E. Morel
Los Alamos National Laboratory, MS D409, Los Alamos, New Mexico 87545
(Received 27 May 1997)

In this paper we apply the simplified spherical harmonic (SP_N) approximation to coupled electron-photon transport problems in two-dimensional cylindrical geometry in the energy range from roughly 10 keV to 10 MeV. The SP_N equations represent an asymptotic approximation that does not necessarily converge to the exact transport solution as $N\rightarrow\infty$, but can sometimes produce solutions that are much more accurate than diffusion theory at a fraction of the cost of a full transport treatment. To our knowledge, the SP_N approximation has previously been applied only to neutron transport problems. We investigate the applicability of the SP_N method to satellite electronics shielding calculations. In addition to applying the approximation, we generalize certain iterative convergence acceleration techniques originally developed for the one-dimensional S_N (discrete ordinates) equations, and apply them to the two-dimensional SP_N equations. We present numerical comparisons with Monte Carlo calculations for the purpose of examining both the accuracy of the SP_N approximation and the computational efficiency of our solution techniques. [S1063-651X(98)04505-X]

PACS number(s): 02.70.−c, 95.30.Jx

I. PURPOSE

The purpose of this paper is investigate the applicability of the simplified spherical harmonic approximation [1] to two-dimensional (2D) coupled electron-photon transport problems in the energy range from approximately 10 keV to 10 MeV. We focus on calculations related to the shielding of satellite electronics from geomagnetically trapped electrons. In addition, we investigate the applicability of certain numerical solution techniques to the SP_N equations that were originally developed for 1D S_N (discrete ordinates) [2] transport calculations.

II. BACKGROUND

The standard spherical harmonic or P_N equations [2] have been used to approximate the Boltzmann transport equation for over fifty years. This approximation is based upon the assumption that the angular dependence of the angular flux can be represented in a truncated spherical harmonic expansion. This expansion is substituted into the transport equation, and angular moments are taken with respect to each spherical harmonic function. This results in a finite system of equations for the angular moments of the angular flux. The index ''N'' in P_N denotes the order of the spherical harmonic expansion. In general, as $N\rightarrow\infty$, the solution of the P_N equations converges to the solution of the transport equation. In multidimensional problems, the P_N equations are quite complex and have a large number of unknowns. For instance, in multidimensional calculations, the number of angular unknowns (moments) is of order N^2. The number of unknowns associated with high expansion orders is particularly significant for electron transport calculations because electron scattering is highly anisotropic and thus often requires high order flux and cross section expansions, e.g., P_7 to P_{15}. The multidimensional P_N method can be prohibitively expensive with such high expansion orders in terms of both memory and CPU time.

In the early 1960s, multidimensional P_N calculations were far beyond the reach of existing computers, but diffusion theory was not always adequate for nuclear reactor analysis. In view of this, Gelbard developed a heuristic simplification of the P_N equations, which he called the simplified P_N equations [1], with the intent that they yield greater accuracy than diffusion theory at a computational cost far less than full P_N theory. The method was originally applied to neutron transport problems, and was observed to give precisely the type of accuracy that Gelbard had hoped for. Since they represented a heuristic simplification to the P_N equations, the SP_N equations were not expected to yield the exact transport equation in the limit as $N\rightarrow\infty$, and they did not do so. The initial derivation of the SP_N equations was neither mathematically rigorous nor physically intuitive. Thus even though Gelbard was able to demonstrate that the SP_N equations were useful, the lack of a sound theoretical foundation has undoubtedly acted as an obstruction to the widespread use of these equations. However, it has recently been shown by Larsen *et al.* that the SP_N equations can be derived from the transport equation via a formal asymptotic expansion related to the diffusion limit [3,4]. Thus a rigorous theoretical basis for the SP_N equations now exists.

Some insight into the accuracy of the SP_N approximation can be gained by considering some of its properties.

(1) The SP_1 and P_1 equations are completely equivalent in all geometries. If $N>1$, there is no equivalence between the SP_N and P_N equations in multidimensional geometries.
(2) The SP_N equations and the P_N equations are completely equivalent in 1D slab geometry.
(3) The multidimensional SP_N equations will exactly yield any P_N solution that has a 1D slab geometry dependence regardless of the orientation of that dependence with respect to the multidimensional coordinate system.

The first property ensures that the diffusion limit is embedded within the SP_N equations. This follows from the fact that the steady-state P_1 equations are equivalent to diffusion theory under the assumption of isotropic scattering. The sec-

 © 1998 The American Physical Society

ond and third properties suggest that if N is sufficiently large, the multidimensional SP_N equations should be very accurate whenever the transport solution is ''locally 1D,'' i.e., whenever the angular flux solution at each point in space has approximately 1D angular and spatial dependencies. For instance, suppose that at each point in space, denoted by $\vec{r}_0$, we can define a direction vector, denoted by $\vec{n}_0$, such that the angular dependence of the angular flux is azimuthally symmetric about $\vec{n}_0$, and the spatial dependence of the angular flux does not vary in any direction perpendicular to $\vec{n}_0$. Then the solution is locally 1D. Furthermore, if the vector $\vec{n}_0$ is constant throughout space, the solution is globally 1D. Pomraning has recently shown that the SP_N equations can be derived both variationally and asymptotically under the assumption that the flux is locally 1D [5]. This derivation requires more restrictive assumptions than that of Larsen *et al.* [3], but it provides a much clearer physical interpretation of the SP_N approximation.

Some insight into the relative cost of the SP_N approximation can be gained by noting that the number of P_N unknowns in multidimensions is of order N^2 whereas the number of SP_N unknowns in multidimensions is of order N. Thus the potential exists for tremendous computational savings when N is large. As previously noted, large values N are often required in electron transport calculations because of the highly anisotropic character of electron scattering.

It has recently been shown that the SP_N equations can be placed in a so-called ''canonical'' form [3,4] that consists of $(N+1)/2$ diffusion equations coupled at each point in space and energy only through a scattering source. These equations can be efficiently solved by iterating upon this source coupling in conjunction with convergence acceleration techniques. The convergence acceleration techniques that we employ are based upon the use of diffusion approximations to estimate iterative errors. The advantage of this approach is that each SP_N iteration consists of solving $(N+1)/2$ independent diffusion equations. The numerical discretization and solution techniques for diffusion equations are highly advanced because of the widespread use of diffusion approximations in physics and engineering. Discretization and solution techniques for the P_N equations are much less advanced.

The diffusion-based iterative convergence acceleration techniques that we apply to the SP_N equations are 2D generalizations of techniques originally developed for the 1D S_N equations. The S_N approximation is currently the most widely used numerical technique for solving the transport equation [2]. Like the P_N method, the S_N method converges to the exact transport solution as $N \rightarrow \infty$. In 1D slab geometry, the S_N equations with Gauss quadrature are equivalent to the P_{N-1} equations. They are also nearly equivalent in other 1D geometries. However, in multidimensional geometries, the S_N and P_{N-1} approximations fundamentally differ. In particular, the P_N equations yield an elliptic approximation for the streaming operator and preserve the rotational invariance of the transport operator, while the S_N equations yield a hyperbolic approximation for the streaming operator and do not preserve this invariance. As a result, S_N solutions can sometimes exhibit nonphysical oscillations called ray effects [2]. The SP_N equations are similar to the P_N equations in that they are elliptic and rotationally invariant, and thus do not exhibit ray effects.

Since the SP_N equations are equivalent to the P_N equations in 1D slab geometry, and the P_{N-1} equations are equivalent to the S_N equations in 1D slab geometry, it follows that the SP_{N-1} equations are also equivalent to the S_N equations in 1D slab geometry. In fact, the ''canonical form'' of the SP_{N-1} equations that we solve reduces exactly to the even-parity S_N equations [6] in 1D slab geometry. Furthermore, the basic iterative solution technique that we use to solve our SP_N equations is the standard source iteration technique [2] routinely used to solve the S_N equations in all geometries. The iterative convergence acceleration techniques that we apply to the SP_N equations are 2D generalizations of the P_1 diffusion-synthetic acceleration technique (P_1-DSA) [7] and the angular multigrid acceleration technique (AMG) [8]. Although P_1-DSA is very effective in 1D S_N calculations, it has recently been shown to be unstable when applied to the 2D S_N equations with highly anisotropic scattering [9]. Since P_1-DSA is a fundamental part of the overall AMG algorithm, it follows that the AMG method will also be unstable under similar conditions. These results are particularly disturbing for electron transport calculations because electron scattering is indeed highly forward peaked, and convergence acceleration is generally needed for electron transport calculations.

We have performed a Fourier analysis that indicates that the P_1-DSA method is as effective for the 2D SP_N equations as it is for the 1D S_N equations. We do not present the details of this analysis here because it is quite lengthy and it is presented elsewhere [10]. However, we do present computational results that demonstrate that *both* the P_1-DSA and AMG techniques are as effective for the 2D SP_N equations as they are for the 1D S_N and S_N equations. This is a somewhat surprising result that enables us to make the SP_N method even more efficient for multidimensional calculations.

In this paper we apply the SP_N approximation to coupled electron-photon transport problems related to shielding satellite electronics from geomagnetically trapped electrons. One would expect that the SP_N approximation would do well in this regime because the exteriors of the satellites are bathed in a uniform isotropic flux of electrons, leading to angular flux distributions that are approximately locally 1D.

The remainder of this paper is organized as follows. First, we describe the Boltzmann transport equations for coupled electron-photon transport, and the cross section data that we use in our SP_N calculations. Next, we describe the SP_N equations that we solve. This is followed by a description of the source iteration technique and the convergence acceleration techniques that we use to solve the SP_N equations. Computational results are presented next. In particular, we compare the SP_N and Monte Carlo methods in terms of both accuracy and computational cost. After some preliminary 1D calculations, calculations are carried out in 2D cylindrical geometry. We do not compare the SP_N method with the P_N and S_N methods because computer codes that can perform coupled electron-photon 2D S_N and P_N calculations in cylindrical geometry (if they exist) are not generally available to the scientific community. On the other hand, Monte Carlo

codes, which represent the accepted standard for multidimensional coupled electron-photon transport calculations, are available from several sources. For instance, we have used a code distributed by Sandia National Laboratories [11]. Finally, our computational results are followed by conclusions and recommendations for future work.

III. COUPLED ELECTRON-PHOTON TRANSPORT EQUATIONS

The fundamental model of particle transport for a system of electrons and photons is given by a Boltzmann-Fokker-Planck (BFP) equation [12] for electrons and the Boltzmann equation [2] for photons. The particular version of BFP equation that we use consists of the Boltzmann equation with an additional continuous-slowing-down term. We refer to this electron equation as the Boltzmann-CSD equation. Coupling occurs between the electron and photon equations due to the physical fact that electrons generate photons in their interaction with the host medium, and photons in turn generate electrons in their interaction with the host medium. We assume that there are no external electric or magnetic fields, and the density of transporting particles is much less than the density of target atoms. The steady-state electron and photon equations are given as

$$\begin{aligned}\vec{\Omega}\cdot\vec{\nabla}\psi_e(\vec{r},E,\vec{\Omega})+\sigma_{te}(\vec{r},E)\psi_e(\vec{r},E,\vec{\Omega})&\\ =\int_0^\infty dE'\int_{4\pi}d\Omega'\sigma^*_{e\to e}(\vec{r},E'\to E,\vec{\Omega}'\cdot\vec{\Omega})\psi_e(\vec{r},E',\vec{\Omega}')&\\ +\int_0^\infty dE'\int_{4\pi}d\Omega'\sigma_{p\to e}(\vec{r},E'\to E,\vec{\Omega}'\cdot\vec{\Omega})&\\ \times\psi_p(\vec{r},E',\vec{\Omega}')+\frac{\partial}{\partial E}\left[R_e(\vec{r},E)\psi_e(\vec{r},E,\vec{\Omega})\right]&\\ +Q_e(\vec{r},E,\vec{\Omega}),&\end{aligned}\tag{1}$$

$$\begin{aligned}\vec{\Omega}\cdot\vec{\nabla}\psi_p(\vec{r},E,\vec{\Omega})+\sigma_{tp}(\vec{r},E)\psi_p(\vec{r},E,\vec{\Omega})&\\ =\int_0^\infty dE'\int_{4\pi}d\Omega'\sigma_{p\to p}(\vec{r},E'\to E,\vec{\Omega}'\cdot\vec{\Omega})\psi_p(\vec{r},E',\vec{\Omega}')&\\ +\int_0^\infty dE'\int_{4\pi}d\Omega'\sigma_{e\to p}(\vec{r},E'\to E,\vec{\Omega}'\cdot\vec{\Omega})&\\ \times\psi_e(\vec{r},E',\vec{\Omega}')+Q_p(\vec{r},E,\vec{\Omega})&\end{aligned}\tag{2}$$

where $\psi(\vec{r},E,\vec{\Omega})$ is the angular flux (in particles $\mathrm{cm}^{-2}\,\mathrm{s}^{-1}\,\mathrm{MeV}^{-1}$), $\vec{\Omega}$ is the particle direction, $\sigma_t(\vec{r},E)$ is the total cross section (in cm^{-1}), and $\sigma^*_{e\to e}(\vec{r},E'\to E,\vec{\Omega}'\cdot\vec{\Omega})$ is the electron to electron differential scattering and production cross section, where E' denotes the initial particle energy, $\vec{\Omega}'$ denotes the initial particle direction, E denotes the final particle direction, and $\vec{\Omega}$ denotes the final direction. This term does not include energy losses due to soft inelastic interactions, which are treated by the CSD operator ($\mathrm{cm}^{-1}\,\mathrm{MeV}^{-1}\,\mathrm{sr}^{-1}$). In addition, $\sigma_{p\to e}(\vec{r},E'\to E,\vec{\Omega}'\cdot\vec{\Omega})$ is the photon to electron differential scattering cross section ($\mathrm{cm}^{-1}\,\mathrm{MeV}^{-1}\,\mathrm{sr}^{-1}$), $\sigma_{p\to p}(\vec{r},E'\to E,\vec{\Omega}'\cdot\vec{\Omega})$ is the photon to photon differential scattering cross section ($\mathrm{cm}^{-1}\,\mathrm{MeV}^{-1}\,\mathrm{sr}^{-1}$), $\sigma_{e\to p}(\vec{r},E'\to E,\vec{\Omega}'\cdot\vec{\Omega})$ is the electron to photon differential scattering cross section ($\mathrm{cm}^{-1}\,\mathrm{MeV}^{-1}\,\mathrm{sr}^{-1}$), $R_e(\vec{r},E)$ is the electron restricted stopping power. Includes only energy losses due to soft inelastic interactions ($\mathrm{cm}^{-1}\,\mathrm{MeV}$), and $Q(\vec{r},E)$ is the distributed angular source (in particles $\mathrm{cm}^3\,\mathrm{s}^{-1}\,\mathrm{MeV}^{-1}$), and subscripts e and p denote electron and photons, respectively.

The electron inelastic interactions (both collisional and radiative) are divided into two classes: ''catastrophic'' interactions that result in large energy losses and directional changes, and ''soft'' interactions that result in small energy losses and directional changes. All catastrophic interactions and the directional changes due to soft interactions are treated with the Boltzmann operator. All energy losses due to soft interactions are treated with the continuous-slowing-down (CSD) operator, i.e., the energy derivative term appearing in Eq. (1). This operator continuously slows down particles at a rate given by the restricted stopping power, R. The stopping power is ''restricted'' in the sense that it includes only contributions from soft interactions.

The CEPXS code [13] was used to generate electron and photon cross-section data for our SP_N calculations. CEPXS produces a special ''pseudo'' cross section [14] that effectively lumps the CSD operator together with the previously defined electron to electron differential scattering cross section, $\sigma^*_{e\to e}$. Thus, the computer code that we developed was designed to solve the SP_N analog of the following pure Boltzmann equations for the electrons and photons:

$$\begin{aligned}\vec{\Omega}\cdot\vec{\nabla}\psi_e(\vec{r},E,\vec{\Omega})+\sigma_{te}(\vec{r},E)\psi_e(\vec{r},E,\vec{\Omega})&\\ =\int_0^\infty dE'\int_{4\pi}d\Omega'\sigma_{e\to e}(\vec{r},E'\to E,\vec{\Omega}'\cdot\vec{\Omega})\psi_e(\vec{r},E',\vec{\Omega}')&\\ +\int_0^\infty dE'\int_{4\pi}d\Omega'\sigma_{p\to e}(\vec{r},E'\to E,\vec{\Omega}'\cdot\vec{\Omega})&\\ \times\psi_p(\vec{r},E',\vec{\Omega}')+Q_e(\vec{r},E,\vec{\Omega}),&\end{aligned}\tag{3}$$

$$\begin{aligned}\vec{\Omega}\cdot\vec{\nabla}\psi_p(\vec{r},E,\vec{\Omega})+\sigma_{tp}(\vec{r},E)\psi_p(\vec{r},E,\vec{\Omega})&\\ =\int_0^\infty dE'\int_{4\pi}d\vec{\Omega}'\sigma_{p\to p}(\vec{r},E'\to E,\vec{\Omega}'\cdot\vec{\Omega})\psi_p(\vec{r},E',\vec{\Omega}')&\\ +\int_0^\infty dE'\int_{4\pi}d\vec{\Omega}\sigma_{e\to p}(\vec{r},E'\to E,\vec{\Omega}'\cdot\vec{\Omega})\psi_e(\vec{r},E',\vec{\Omega}')&\\ +Q_p(\vec{r},E,\vec{\Omega}).&\end{aligned}\tag{4}$$

However, it is important to recognize that the actual electron equation being solved includes the CSD term. The CSD term is simply ''embedded'' within the electron to electron differential scattering cross section in Eq. (3) via the CEPXS data. This is why we use $\sigma_{e\to e}$ in Eq. (3) rather than $\sigma^*_{e\to e}$.

IV. MULTIGROUP SP_N EQUATIONS

The SP_N equations that we solve are discretized in energy using the standard multigroup approximation [2]. A group is associated with both an interval of energies and a particle type. For instance, in a typical calculation, groups 1 through 50 might represent 50 contiguous energy intervals for electrons, while groups 51 through 80 might represent 30 contiguous energy intervals for photons. The multigroup angular flux for group g is denoted by ψ_g, and represents the integral of the angular flux over the energy interval associated with group g. The CEPXS code provides data in a multigroup Legendre format. In particular, CEPXS provides the total cross section for each group together with Legendre moments of cross sections for transfers between groups. These data are sufficient to completely describe the interaction of electrons and photons with matter.

The canonical multigroup SP_N equations [4,15] are given as

$$-\mu_m^2\vec{\nabla}\cdot\frac{1}{\sigma_{tg}}\vec{\nabla}\psi_{mg}^{+}+\sigma_{tg}\psi_{mg}^{+}=Q_{mg}^{+}-\mu_m\vec{\nabla}\cdot\left(\frac{\vec{Q}_{mg}^{-}}{\sigma_{tg}}\right),$$
$$m=1,(N+1)/2,\quad g=1,G \tag{5}$$

$$\vec{\psi}_{mg}^{-}=-\frac{\mu_m}{\sigma_{tg}}\vec{\nabla}\psi_{mg}^{+}+\frac{1}{\sigma_{tg}}\vec{Q}_{mg}^{-},$$
$$m=1,(N+1)/2,\quad g=1,G, \tag{6}$$

where

$$Q_{mg}^{+}=\sum_{j=1}^{G}\sum_{n=0,2,}^{N-1}(2n+1)P_n(\mu_m)\sigma_{n,j\to g}\phi_{nj}+g_{mg}^{+}, \tag{7}$$

$$\vec{Q}_{mg}^{-}=\sum_{j=1}^{G}\sum_{n=1,3,}^{N}(2n+1)P_n(\mu_m)\sigma_{n,j\to g}\vec{\phi}_{n,j}+\vec{q}_{mg}^{-}, \tag{8}$$

$$\phi_{ng}=2\sum_{m=1}^{(N+1)/2}P_n(\mu_m)\psi_{mg}^{+}w_m,\quad n\ \text{even}, \tag{9}$$

$$\vec{\phi}_{ng}=2\sum_{m=1}^{(N+1)/2}P_n(\mu_m)\vec{\psi}_{mg}^{-}w_m,\quad n\ \text{odd}, \tag{10}$$

and where ψ^{+} and $\vec{\psi}^{-}$ are the SP_N analogs of the even- and odd-parity angular fluxes, m is the angular index, μ_m is the mth Gauss quadrature cosine, w_m is the mth Gauss quadrature weight, $P_n(\mu)$ is the Legendre polynomial of degree n, g is the energy group index, N is an odd integer, ϕ_n is the analog angular flux moment, $\sigma_{n,j\to g}$ is the nth Legendre moment of the cross section for ''scattering'' from group j to group g, q_m^{+} and $\vec{q}_m^{-}$ are the analogs of the even- and odd-parity angular distributed sources, respectively, and all other quantities are as previously defined. Note that in the multigroup approximation, ''scattering'' cross sections may physically represent particle production as well as true scattering.

For the case of 1D slab geometry, the SP_N equations become equivalent to the even-parity S_{N+1} equations and these quantities can be related to the angular flux ψ as follows:

$$\psi^{+}(\mu_m)=\tfrac{1}{2}[\psi(\mu_m)+\psi(-\mu_m)], \tag{11}$$

$$\vec{\psi}^{-}(\mu_m)=\tfrac{1}{2}[\psi(\mu_m)-\psi(-\mu_m)]\vec{n}, \tag{12}$$

where $\vec{n}$ is a unit vector directed along the 1D spatial axis. We henceforth suppress use of the term ''analog'' when referring to the even-parity and odd-parity fluxlike and sourcelike quantities in the SP_N equations.

The canonical SP_N equations are spatially discretized with a standard bilinear-continuous finite element treatment [16] to obtain a set of matrix equations amenable to computational solution. The term $\mu_m\vec{\nabla}\cdot(\vec{Q}_{mg}^{-}/\sigma_{tg})$ on the right side of Eq. (5) would appear to require special attention because such a term does not usually appear in standard diffusion equations. However, the problems that we consider do not have distributed sources. In this case, it can be shown that Q_{mg}^{+} is composed of a linear combination of even-parity flux gradients, and consequently that $\mu_m\vec{\nabla}\cdot(\vec{Q}_{mg}^{-}/\sigma_{tg})$ has the same spatial discretization as the standard term $-\mu_m^2\vec{\nabla}\cdot(1/\sigma_{tg})\vec{\nabla}\psi_{mg}^{+}$ on the left side of Eq. (5).

Because the SP_N equations are self-adjoint, the finite-element treatment yields symmetric positive definite coefficient matrices. Efficient, robust numerical methods exist for the solution of such matrix equations. In particular, we use the conjugate-gradient method preconditioned with incomplete Cholesky decomposition (ICCG) [17] and the black-box multigrid method (BBMG) [18] in conjunction with source iteration to solve the discretized SP_N equations.

V. SOURCE ITERATION

Our multigroup SP_N equations can be solved iteratively by the source iteration (SI) method. This technique is actually quite simple. Note that all coupling in group and direction occur in the scattering sources on the right sides of Eqs. (5) and (6). In its simplest possible form, source iteration proceeds by using the fluxes from the previous iteration to calculate new scattering sources, and then solving Eqs. (5) and (6) to obtain the next flux iterates. The process is then repeated until convergence is achieved. The previous iterate fluxes for the first iteration are generally assumed to be zero unless a better guess is available.

In a multigroup calculation, the source iteration process is decomposed into two nested iterations referred to as the inner and outer iterations. The outer iterations are characterized by iterations on the scattering sources resulting from intergroup transfers, while the inner iterations are characterized by iterations on the scattering sources resulting from within-group transfers. As one would expect from the nomenclature, the inner source iteration is nested within the outer source iteration.

An outer source iteration begins by using the latest flux iterates to calculate the intergroup scattering source for group 1. Next the inner source iteration for group 1 begins by using the latest iterate for the group 1 flux to calculate the within-group scattering source for group 1. The inner iteration for group 1 is completed by solving the equations for the group 1 fluxes. The inner iteration process is then repeated until convergence of the within-group scattering source is achieved for group 1. The outer iteration is completed by performing all of the steps described above for each remain-

ing group in succession. The outer iterations are repeated (together with the inner iterations nested within them) until the intergroup scattering sources converge for all of the groups.

It is useful to consider a formal representation of the inner source iteration process for a single group. In particular,

$$-\mu_m^2 \vec{\nabla}\cdot \frac{1}{\sigma_t}\vec{\nabla}\psi_m^{+(l+1)}+\sigma_t\psi_m^{+(l+1)} = Q_m^{+}-\mu_m^{+(l)}-\mu_m\vec{\nabla}\cdot\left(\frac{\vec{Q}_m^{-(l)}}{\sigma_t}\right), \quad m=1,(N+1)/2, \tag{13}$$

$$\vec{\psi}_m^{-(l+1)} = -\frac{\mu_m}{\sigma_t}\vec{\nabla}\psi_m^{+(l+1)}+\frac{1}{\sigma_t}\vec{Q}_m^{-(l)}, \quad m=1,(N=1)/2, \tag{14}$$

$$\phi_n^{(l+1)} = 2\sum_{m=1}^{N/2} P_n(\mu_m)\psi_m^{+(l+1)}w_m \quad \text{for } n \text{ even}, \tag{15}$$

$$\vec{\phi}_n^{(l+1)} = 2\sum_{m=1}^{N/2} P_n(\mu_m)\vec{\psi}_m^{-(l+1)}w_m \quad \text{for } n \text{ odd}, \tag{16}$$

$$Q_m^{+(l+1)} = \sum_{n=0,2}^{N-1}(2n+1)P_n(\mu_m)\sigma_n\phi_n^{(l+1)}+q_m^{+}, \tag{17}$$

$$\vec{Q}_m^{-(l+1)}+\sum_{n=1,3}^{N}(2n+1)P_n(\mu_m)\sigma_n\vec{\phi}_n^{(l+1)}+\vec{q}_m, \tag{18}$$

where l is the inner iteration index, and where the group indices have been suppressed for simplicity and the intergroup sources have been hidden within the inhomogeneous sources. Let us now review the inner iteration process in detail. The iteration process begins with even-parity and odd-parity angular fluxes from the previous iteration (step l). These flux iterates are used together with Eqs. (15)–(18) to calculate new even-parity and odd-parity sources, $Q_m^{+(l)}$ and $\vec{Q}_m^{-(l)}$, respectively. The inner iteration process proceeds by solving Eq. (13) for the even-parity angular fluxes at step $l+1$ while keeping the scattering sources on the right side of that equation fixed at step l. Note that this step requires the solution of $(N+1)/2$ independent diffusion equations. The inner iteration at step $l+1$ is completed by using the even-parity fluxes at step $l+1$ and the odd-parity sources at step l together with Eq. (14) to obtain the odd-parity angular fluxes at step $l+1$. Note that Eq. (14) constitutes an explicit expression for the odd-parity flux, i.e., one need not solve a differential equation. Rather one need only take a gradient of the even-parity flux.

We solve each of the discrete diffusion equations associated with the discrete version of Eq. (13) using either the incomplete-Cholesky conjugate-gradient (ICCG) method [17] or the black-box multigrid (BBMG) method [18]. Thus there are iterations nested within the inner source iterations. We refer to these iterations as diffusion iterations.

The stopping criteria for the diffusion iterations depend upon the solver being used. For instance, the ICCG solver uses a stopping criterion based upon the relative change of the solution vector together with the norm of the residual relative to the norm of the source vector. Specifically, let us express the equations being solved as follows:

$$C\vec{v}=\vec{b}, \tag{19}$$

where C is the coefficient matrix, $\vec{v}$ is the solution vector, and $\vec{b}$ is the source vector. The ICCG iterations are terminated when

$$\frac{\|\vec{v}^{(l+1)}-\vec{v}^{(l)}\|}{\|\vec{v}^{(l+1)}\|} > \mathcal{T} \tag{20}$$

and

$$\frac{\|C\vec{v}^{(l+1)}-\vec{b}\|}{\|\vec{b}\|} > \mathcal{T}, \tag{21}$$

where ''$\|\ \|$'' denotes the Euclidean vector norm, l denotes the ICCG iteration index, and $\mathcal{T}$ denotes the user-specified error tolerance.

The black-box multigrid solver has its own stopping criteria, but we do not use it. Rather we simply have the BBMG routine perform 5-V cycles and then accept the solution as converged. This seems to be the most efficient way to use the BBMG solver for the class of problems we considered.

The inner source iterations are terminated when the Euclidean norm of the change in the zeroth flux moments divided by the Euclidean norm of the zeroth flux moments is less than a user-specified error tolerance. Specifically, termination occurs when

$$\left(\frac{\Sigma_k|\phi_{0k}^{(l+1)}-\phi_{0k}^{(l)}|^2}{\Sigma_k|\phi_{0k}^{(l+1)}|^2}\right)^{1/2} < \mathcal{T}, \tag{22}$$

where k is the spatial index.

The outer source iterations are terminated using a variation on the condition given in Eq. (22):

$$\left(\frac{\Sigma_k|\phi_{0kg}^{(l+1)}-\phi_{0kg}^{(l)}|^2}{\Sigma_k|\phi_{0kg}^{(l+1)}|^2}\right) < \mathcal{T}, \quad g=1,G, \tag{23}$$

where ϕ_{0kg}^{l} denotes the final zeroth flux moment for space-point k and group g calculated during outer iteration l.

In general, the diffusion iteration convergence criterion is made more stringent than the inner source iteration criterion, and the inner source iteration convergence criterion is made more stringent than the outer source iteration criterion. Optimal stopping criteria are difficult to define. We generally used tolerances of 10^{-6}, 10^{-5}, and 10^{-4}, respectively, for the diffusion iterations, inner source iterations, and outer source iterations. Of course, there was no explicit convergence tolerance for the diffusion iterations when the BBMG method was used to solve Eq. (13).

The outer iterations generally converge quite quickly for coupled electron-photon transport calculations. In fact, because of simplifications to the physics for electron produc-

tion by photons (discussed in Sec. VII), all of the calculations presented in this paper were guaranteed to converge in one outer source iteration.

Inner iterations can be very slow to converge. This is particularly so for the lower-energy electron groups. Thus acceleration of the inner source iteration convergence is highly desirable for these groups.

VI. CONVERGENCE ACCELERATION

We use two related acceleration techniques to accelerate the inner iterations of electrons: P_1 diffusion-synthetic acceleration (P_1-DSA) [7] and the angular multigrid method [8]. The P_1-DSA method can be interpreted as a two-grid method. In fact, P_1-DSA is imbedded within the angular multigrid method. We will explain what we mean by this shortly. Let us begin a description of synthetic acceleration by considering the following general matrix problem

$$\mathbf{H}f=q, \tag{24}$$

which may be solved iteratively by splitting the coefficient matrix

$$\mathbf{H}=\mathbf{A}-\mathbf{B} \tag{25}$$

and specifying an iteration scheme as follows:

$$f^{(l+1)}=\mathbf{A}^{-1}\mathbf{B}f^{(l)}+\mathbf{A}^{-1}q. \tag{26}$$

By manipulating Eqs. (24), (25), and (26), it may be shown that the exact error in f at iteration step $(l+1)$ satisfies

$$\mathbf{H}\boldsymbol{\epsilon}^{(l+1)}=r^{(l+1)}, \tag{27}$$

where the error is defined by

$$\boldsymbol{\epsilon}^{(l+1)}=f-f^{(l+1)} \tag{28}$$

and the residual is defined as

$$r^{(l+1)}=q-\mathbf{H}f^{(l+1)}. \tag{29}$$

We can obtain the exact error in $f^{(l+1)}$ by solving Eq. (27). However, Eq. (27) is just as difficult to solve as the original problem, Eq. (24). The main idea of synthetic acceleration is to obtain an estimate of the error in $f^{(l+1)}$ by solving Eq. (27) with a low-rank approximation to $\mathbf{H}$. The accelerated iteration scheme then takes the form

$$f^{(l+1/2)}=\mathbf{A}^{-1}\mathbf{B}f^{(l)}+\mathbf{A}^{-1}q, \tag{30}$$

$$r^{(l+1/2)}=q-\mathbf{H}f^{(l+1/2)}, \tag{31}$$

$$c^{(l+1/2)}=\mathbf{H}_L^{-1}\mathbf{P}r^{(l+1/2)}, \tag{32}$$

$$f^{(l+1)}=f^{(l+1/2)}+\mathbf{T}c^{(l+1/2)}, \tag{33}$$

where $\mathbf{H}_L$ is a low-rank operator, $\mathbf{P}$ is a projection operator that maps the full-rank residual to the low-rank space of $\mathbf{H}_L$, and $\mathbf{T}$ is an interpolation operator that maps the low-rank correction to the full-rank space of $\mathbf{H}$.

Synthetic acceleration is effective if the following three conditions are met.

(1) The low-rank operator must be inexpensive to invert relative to the cost of inverting the full-rank operator.
(2) The low-rank operator must attenuate the error modes, which are not well attenuated by the basic iteration scheme.
(3) The low-rank operator must not excessively amplify the error modes that are well attenuated by the basic iteration scheme.

In P_1-diffusion synthetic acceleration [7], the basic iteration scheme is source iteration, and the low-rank operator is the P_1 operator. The projection and interpolation operators are defined in terms of P_0 and P_1 Legendre moments of the angular flux. The effectiveness of an iteration scheme is usually measured in terms of its spectral radius. The spectral radius represents the asymptotic error reduction factor, i.e., the factor by which any norm of the error is reduced per iteration after ''sufficiently many'' iterations. In general, the spectral radius values quoted in this paper for various methods will correspond to spatially infinite homogeneous problems with no spatial discretization and in some cases, no angular discretization. The spectral radii observed in realistic discretized computations are usually comparable to the idealized model values as long as one is careful to consistently discretize the low-order operators relative to the high-order operator [19].

Source iteration has an infinite-medium spectral radius equal to the scattering ratio, $c\equiv\sigma_0/\sigma_t$. The spectral radius in any finite-medium problem is bounded from above by the infinite-medium value, and approaches the infinite-medium value as the optical thickness of the finite domain increases. In the worst case, the infinite-medium spectral radius is unity. This corresponds to pure scatter with no removal, i.e., $\sigma_t=\sigma_0$. Electron scattering generally leads to spectral radii for the low-energy groups that are very near unity. Thus source iteration is inefficient for these electron groups. If the scattering cross-section expansions can be accurately truncated at the P_1 level, P_1-DSA reduces the spectral radius to approximately $0.23c$. This is a dramatic improvement for simply solving one additional diffusion equation per group. On the other hand, if higher expansion orders must be used, the spectral radius with P_1-DSA is given by $\beta\equiv\sigma_2/\sigma_t$ [20]. Unfortunately, as the scattering becomes increasingly forward peaked, β approaches unity [8]. Thus P_1-DSA becomes ineffective in the forward-peaked scattering limit.

This deficiency can be remedied by using an angular multigrid method that is in some sense a generalization of the P_1-DSA method. For instance, the P_1-DSA method can be thought of as a two-grid method. The ''fine grid'' is the transport operator (or in our case, the SP_N equations), and the ''coarse grid'' is the P_1 operator. The central theme of a multigrid scheme is to have a hierarchy of increasingly coarse grids. Each coarse grid is used to calculate an estimate of the error on the grid above it. For instance, let us assume that the angular multigrid method starts with an SP_{15} approximation on the ''fine grid.'' A source iteration is performed on this grid to obtain an estimate of the solution. Then the SP_{15} residuals are calculated and projected onto the next coarse grid, which consists of an SP_7 approximation. A source iteration is performed on the SP_7 grid to obtain an estimate of the error on the SP_{15} grid. Then the SP_7 residual is calculated and projected onto an SP_3 grid. A source itera-

tion is performed on the SP_3 grid to obtain an estimate of the error on the SP_7 grid. The SP_3 residual is then calculated and projected onto an SP_1 grid. The SP_1 equations are then solved to obtain an estimate of the error on the SP_3 grid. This SP_1 estimate is then interpolated onto the SP_3 grid and added to the SP_3 iterate to obtain an improved SP_3 estimate for the error in the SP_7 grid. This SP_3 estimate is then interpolated onto the SP_7 grid and added to the SP_7 iterate to obtain an improved SP_7 estimate of the error on the SP_{15} grid. Finally, this SP_7 estimate is then interpolated onto the SP_{15} grid and added to the SP_{15} iterate to obtain an improved estimate for the SP_{15} solution. This constitutes one AMG iteration. Obtaining solutions on all of these grids would seem to be extremely expensive, but it can be shown that all of the coarse grid source iterations cost roughly the same as a single fine grid source iteration in the limit as $N \rightarrow \infty$. In the forward-peaked scattering limit, the spectral radius for the AMG algorithm approaches 0.56 whereas the P_1-DSA spectral radius approaches unity. This scheme is extremely efficient as long as the SP_1 equations can be efficiently solved. In general, one finds that the AMG method becomes increasingly effective relative to P_1-DSA method in electron transport calculations in the limit as the SP_N order increases. The exact reasons for this effect are well understood [8], but too complicated to explain in detail here. It is related to the fact that forward-peaked cross-section moments are modified in S_N and SP_N calculations using the extended transport correction [21] to reduce the spectral radius of the pure source iteration process without altering the solution of the equations [8]. As a result, the effective anisotropy of the cross-section expansions increases with increasing N even though the anisotropy of the physical cross sections obviously does not vary.

Note that if we eliminate all of the coarse grids except the SP_1 grid, we get the P_1-DSA algorithm (the SP_1 and P_1 approximations are always identical). This is why we previously stated that the P_1-DSA method is imbedded in the AMG method.

Our computational results indicate that the spectral radius values that we have given for the P_1-DSA and AMG methods are valid when these schemes are applied to the SP_N equations in one or two spatial dimensions, and we suspect that they are valid in three spatial dimensions as well. However, when these methods are applied to the S_N equations, the spectral radius values that we have given are valid only in one spatial dimension. As previously noted, both the P_1-DSA and AMG methods can become unstable when applied to the S_N equations in two spatial dimensions if the scattering is sufficiently forward-peaked and the scattering ratio is sufficiently high. A demonstration of the applicability of the P_1-DSA and AMG methods to multidimensional SP_N calculations is an important component of this paper.

VII. COMPUTATIONAL RESULTS

To determine the accuracy and efficiency of our SP_N method for satellite shielding applications, we formulated both 1D and 2D test problems. We performed SP_N calculations using a code written by one of the authors (Josef). To provide a standard of comparison, we also performed calculations using the Monte Carlo code CYLTRAN [11]. CYLTRAN is accepted by the scientific community as an accurate state-of-the-art code for coupled electron-photon transport calculations. Thus it is appropriate that it serve as our benchmark. For each problem we investigate the accuracy of the numerical solutions, the computational efficiency of the methods, and provide a brief discussion of results. We have compared our SP_N scheme with an unbiased Monte Carlo method. The CYLTRAN code can be biased to more efficiently perform coupled electron-photon transport calculations, but one must be sufficiently expert in both Monte Carlo methods and the CYLTRAN code itself to implement appropriate variance-reduction schemes. The casual user must be content to run the code without biasing. Ideally, we would have preferred to compare our SP_N algorithm with a 2D R-Z geometry S_N algorithm. However, to our knowledge, only 1D coupled electron-photon S_N codes are available to the community at the present time [22].

All Monte Carlo results given in this paper include a statistical uncertainty, e.g., $5.6 \pm 2\%$. The uncertainty represents one standard deviation expressed as a percentage of the solution. Thus the answer of 5.6 given in the previous example has a standard deviation of $5.6 \times 0.02 = 0.122$.

All calculations were performed using an option in the CEPXS [13] code that suppresses the generation of electrons by photons. Any photon energy that would have gone into electrons is locally deposited in the material at the point of the photon interaction. This is a good approximation for the space shielding calculations that we have performed. Specifically, inclusion of the full physics generally changes the solution by no more than a percent or so. This option is economical because we would otherwise have to include positron groups due to pair production. Furthermore, since the electron groups come first in the group structure, the group-to-group scattering matrix has a lower-triangular structure. Thus only one outer source iteration is required. Overall, this option saves roughly a factor of two in memory and CPU time.

All calculations were performed on a CRAY YMP computer at Los Alamos National Laboratory.

A. Test problem one

We begin with a simple homogeneous problem in 1D slab geometry. The purpose of this problem is to establish the level of agreement achieved between the SP_N and Monte Carlo (MC) methods when the problem is simple and the

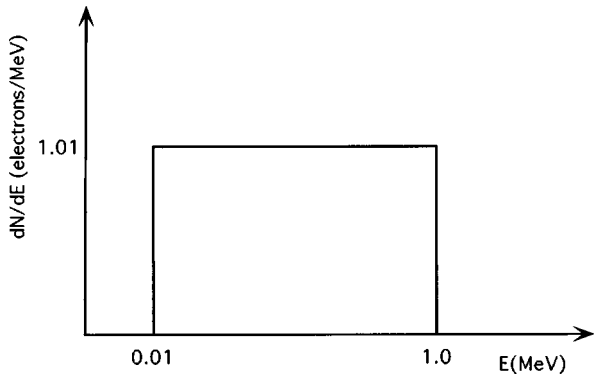

FIG. 1. Problem one: Electron differential spectrum.

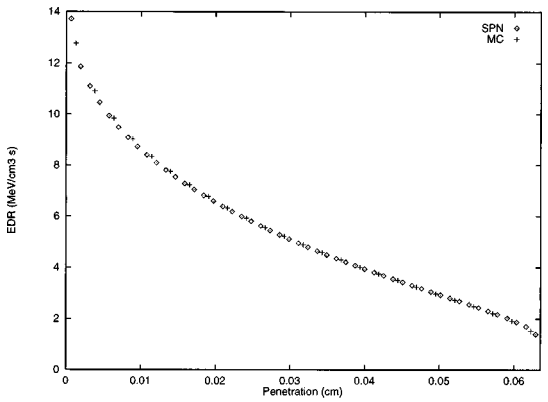

FIG. 2. Problem one: energy deposition rate vs penetration.

SP_N method is convergent. The problem consists of a 1D homogeneous aluminum slab with an isotropic boundary source of electrons (1 electron/cm^2 s). The slab has a thickness of 25 mils (0.0635 cm), with the source located at the plane $z=0$ cm. The source electrons are distributed in a flat energy spectrum as shown in Fig. 1. We have calculated the energy deposition rate (EDR) as a function of penetration, and the energy deposition rate in a test region defined by 24 mil$\leqslant z \leqslant$25 mil. We have performed an SP_{15} calculation with 80 energy groups ($50e^-$, 30γ) and 50 spatial cells of uniform mesh spacing ($\Delta z = 1.27\times 10^{-3}$ cm). We performed a Monte Carlo calculation with 10^6 source electron histories. The SP_N and Monte Carlo results for the EDR profile are compared in Fig. 2. Note that these profiles are almost identical. The SP_N and Monte Carlo CPU times together with the results for the EDR in the test region are given in Table I. We note that the test region energy deposition rates differ less than 2%, and the SP_N method is over 200 times faster than the unbiased Monte Carlo method.

B. Test problem two

The second problem we consider is a 1D multimaterial deep penetration problem. Deep penetration problems are problems in which the source electrons are highly attenuated before reaching the region within which the dose is desired. The purpose of this problem is to establish the level of agreement achieved between the SP_N and Monte Carlo methods when the problem is difficult and the SP_N method is convergent. The geometry is shown in Fig. 3. An isotropic geosynchronous trapped electron source [23], described in Table II, is incident at the plane $z=0$ cm. The source is normalized to 1 particle/cm^2 s. This source-geometry configuration is characteristic of space shielding benchmark problems [23], with the silicon region representing a semiconductor device, and the aluminum and tungsten regions representing the shield. We have written a FORTRAN code to produce the SP_N and Monte Carlo input spectrum from the tabular electron spectra

TABLE I. Problem one: results for test region.

	EDR (MeV/cm^3 s)	CPU time
SP_{15}	1.55	41 *s*
MC	1.52±1%	2 hr 22 min

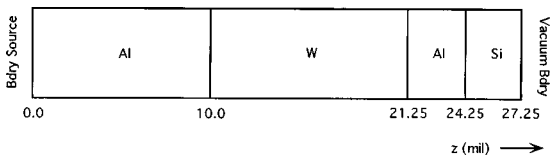

FIG. 3. Problem two: geometry.

data. We have performed SP_1, SP_3, SP_7, and SP_{15} calculations, each with 70 spatial cells having the following cell widths in the respective material regions: $\Delta_{\mathrm{Al,Si}} = 1.27\times 10^{-3}$ cm, $\Delta_W = 7.5197\times 10^{-4}$ cm. To obtain low standard statistical errors for the Monte Carlo solution, it was necessary to run a large number of source electron histories (1×10^7). The calculated EDR in the silicon region is given together with CPU times in Table III for both the SP_N and Monte Carlo calculations.

Note from Table III that the largest change in the solution occurs between SP_1 and SP_3. After SP_7 the solution changes relatively little, while the required CPU time increases in proportion to the approximation order N. The SP_{15} and Monte Carlo results differ by 5%, with the Monte Carlo CPU time exceeding the SP_{15} CPU time by over two orders of magnitude.

To confirm that this is a deep penetration problem, we have calculated the unshielded or free space dose to the silicon region. This value was found to be 12.0 MeV/cm^3 s, indicating 4 orders of magnitude attenuation by the shield. Thus the silicon region is indeed highly shielded.

C. Test problem three

The third problem is a 2D, R-Z geometry, four region, deep penetration problem. The geometry is shown in Fig. 4. Each region represents a coaxial cylinder of uniform composition. A geosynchronous trapped electron source is uniformly incident along the outer periphery. Again, this geometry-source configuration is characteristic of satellite

TABLE II. Geosynchronous electron spectrum.

Energy (MeV)	Integral spectrum[a] (e/cm^2)	Differential spectrum (e/cm^2 MeV)
0.1	1.878 [12][b]	1.227 [13]
0.5	2.789 [11]	1.047 [12]
1.0	5.861 [10]	1.661 [11]
1.5	1.375 [10]	4.082 [10]
2.0	3.224 [09]	8.685 [09]
2.5	8.832 [08]	2.409 [09]
3.0	2.419 [08]	4.678 [08]
3.5	1.313 [08]	1.278 [08]
4.0	7.122 [07]	1.074 [08]
4.5	3.153 [07]	4.899 [07]
5.0	1.396 [07]	2.868 [07]
5.5	3.862 [06]	1.092 [07]
6.0	1.069 [06]	2.194 [06]

[a]The integral spectrum is given for a period of one day. The integral spectrum value at energy E_i is defined as the integral spectrum between energies E_i and ∞.

[b]Value should be read as 1.878×10^{12}.

TABLE III. Problem two: results.

	EDR (MeV/cm^3 s)	CPU time
SP_1	1.67×10^{-3}	09 s
SP_3	2.02×10^{-3}	20 s
SP_7	2.11×10^{-3}	45 s
SP_{15}	2.14×10^{-3}	91 s
MC	$2.26\times10^{-3}\pm3\%$	6 hr 4 min

shielding benchmark problems. We note that for the calculation of the dose in a region deep within a multidimensional problem, the Monte Carlo method requires a large number of histories and often a corresponding large CPU time. We have performed SP_1, SP_3, and SP_7 calculations, using a 35 $\times$35 spatial mesh having the following cell widths in each material region: $\Delta_{\mathrm{Al,Si}}=2.54\times10^{-3}$ cm, $\Delta_w=1.504\times10^{-3}$ cm. For the Monte Carlo calculation we have run 2×10^7 source electron histories. The EDR in the silicon region and the CPU times for both the SP_N and Monte Carlo calculations are given in Table IV.

Note from Table IV that the largest change in the solution once again occurs between SP_1 and SP_3, with a relatively small change between SP_3 and SP_7. The SP_7 and Monte Carlo results differ by 8%, with the Monte Carlo CPU time exceeding the SP_7 CPU time by over two orders of magnitude. The SP_7 solution significantly overshoots the Monte Carlo solution. However, there is also a relatively large uncertainty of 8% in the Monte Carlo answer. Unfortunately, the current Monte Carlo calculation required over 9 h. To reduce the uncertainty to 4% would require an excessive run time of 37 h. It is certainly possible for SP_N solutions to overshoot the true solution. For instance, such overshoots have been observed in previous neutral-particle SP_N studies [15]. Since it was not practical to improve the Monte Carlo statistics by running more particles, we reduced the dimensions of the problem so that an uncertainty of 2% could be achieved with only 5×10^6 source histories. The SP_7 solution overshoots the Monte Carlo solution by about 7% for

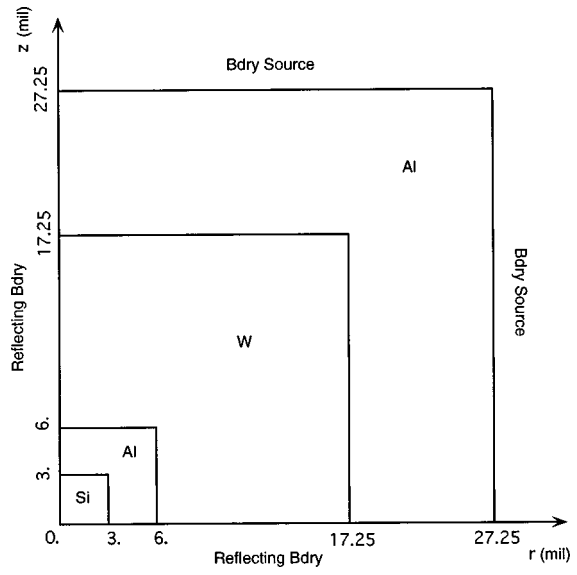

FIG. 4. Problem three: geometry.

TABLE IV. Problem three: results.

	EDR (MeV/cm^3 s)	CPU time
SP_1	1.60×10^{-2}	63 s
SP_3	1.93×10^{-2}	138 s
SP_7	1.97×10^{-2}	286 s
MC	$1.82\times10^{-2}\pm8\%$	9 h 22 min

this modified problem. Thus the 8% overshoot observed in the original problem is probably real.

To confirm that this problem is a deep penetration problem, we calculated the unshielded or free space dose to the silicon region. It was found to be 25.8 MeV/cm^3 s while the Monte Carlo calculation gave a shielded dose of 1.82×10^{-2}, indicating 3 orders of magnitude attenuation by the shield. Thus the silicon region is indeed highly shielded.

The computational efficiency of the SP_N code for problem three with various acceleration schemes and two different diffusion solvers is displayed in Table V. In this particular calculation, the AMG scheme with a preconditioned conjugate gradient (ICCG) diffusion solver [17] is shown to be the most efficient. However, if the problem is sufficiently ill conditioned, the multigrid (BBMG) diffusion solver [18] can surpass the conjugate gradient solver in efficiency. We later give an example of such a problem. We stress that the ICCG and BBMG methods are used to solve the source iteration equations [which take the form of diffusion equations, i.e., see Eq. (13)] and are not to be confused with the P_1-DSA and AMG methods used to accelerate the source iterations.

D. Problem four

We have performed a series of calculations to further investigate the effectiveness of the angular multigrid method (AMG) when applied to 2D SP_N calculations. In particular, we compare the computational spectral radii of the 1D and 2D SP_N methods with the computational spectral radius of the one-dimensional S_N method for one group problems with highly forward peaked Fokker-Planck scattering [8]. The 1D problem consists of a homogeneous, nonabsorbing slab that is 10 transport mean free paths thick with an isotropic distributed source and vacuum boundary conditions on both boundaries. The 2D problem used for the comparison represents a generalization of a 1D problem defined by Morel and Manteuffel [8]. In particular, the 2D generalization was trivially obtained by making the problem domain a square in Cartesian geometry having the same length on each side as the length of the 1D problem, with vacuum boundary conditions prescribed at all boundaries.

TABLE V. Problem three: SP_N acceleration scheme performance.

Acceleration scheme	Matrix solver	CPU time (s)
None	ICCG	891
P_1-DSA all groups	ICCG	414
AMG e^- groups, P_1-DSA γ groups	ICCG	286
AMG e^- groups, P_1-DSA γ groups	MG	310

TABLE VI. Performance of angular multigrid and diffusion synthetic methods.

Acceleration	N	1D S_{N+1} Spectral radius	1D SP_N Spectral radius	2D SP_N Spectral radius
AMG	3	0.36	0.35	0.35
P_1-DSA	3	0.36	0.35	0.35
AMG	7	0.47	0.47	0.47
P_1-DSA	7	0.81	0.81	0.82
AMG	15	0.54	0.54	0.54
P_1-DSA	15	0.95	0.95	0.95

The spectral radius can be computationally estimated at inner source iteration step l as follows [8]:

$$\rho^{(l+1)}=\left(\frac{\Sigma_{nk}|\phi_{nk}^{(l+1)}-\phi_{nk}^{(l)}|^2}{\Sigma_{nk}|\phi_{nk}^{(l)}-\phi_{nk}^{(l-1)}|^2}\right)^{1/2}, \tag{34}$$

where n and k represent the moment and spatial indices, respectively. The Legendre moments for the Fokker-Planck scattering assumed in this problem are given by [8]

$$\sigma_n=\frac{\alpha}{2}[N(N-1)-n(n+1)], \quad n=0,1,\ldots,N-1 \tag{35}$$

for an SP_N calculation. Note that the expansion coefficients depend upon the parameter N, i.e., an SP_3 calculation uses different expansion coefficients than an SP_5 calculation.

As previously noted, the SP_N equations are equivalent to the S_{N+1} equations in one dimension. However, the SP_N equations that we solve in 1D are equivalent to the 1D even-parity form of the S_{N+1} equations rather than the standard first-order form solved in Morel and Manteuffel [8]. Nonetheless, it can be shown that the source iteration process is equivalent for both the even-parity and first-order forms of the S_N equations [6]. Thus, we would expect to see the same spectral radius in 1D SP_N calculations as in the 1D S_N calculations presented in Ref. [8]. Our previous Fourier analysis [10] indicated that the P_1 diffusion synthetic acceleration scheme exhibits exactly the same effectiveness on 2D SP_N calculations that it does on 1D SP_N calculations. This would suggest that AMG should have the same effectiveness on 2D SP_N calculations as 1D S_{N+1} calculations. Finally, we wish to remind the reader that both the P_1-DSA and AMG methods are unstable (with sufficiently forward-peaked scattering and sufficiently small absorption) for 2D S_N calculations, yet are both very effective for one-dimensional S_N calculations. The 2D generalization of the Morel-Manteuffel problem has the required characteristics to make the P_1-DSA and AMG methods unstable when applied to the S_N equations. The results of our investigation are given in Table VI. Note from Table VI that the 1D results are identical for the S_{N+1} and SP_N calculations. Furthermore, the 1D and 2D SP_N results are identical. Therefore, we conclude that the angular multigrid method exhibits exactly the same effectiveness on 2D SP_N calculations that it does for 1D SP_N calculations.

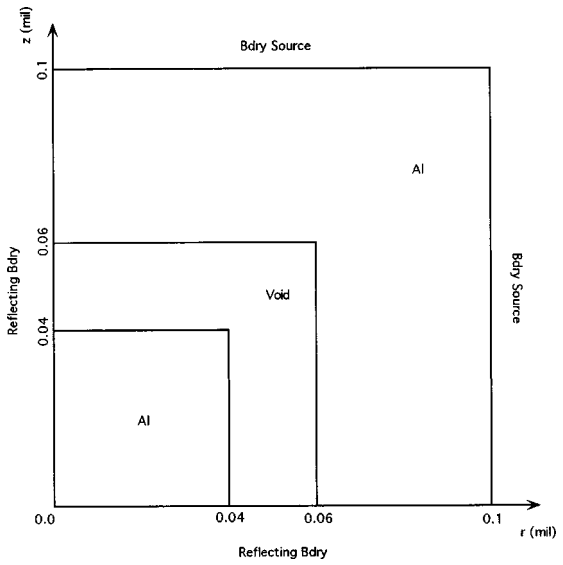

FIG. 5. Problem five: geometry.

E. Test problem five

The fifth problem is a 2D, R-Z geometry, three region problem with a void region. The problem geometry is shown in Fig. 5. This geometry-source configuration is characteristic of the satellite shielding benchmark problems defined by Saqui *et al.* [23]. Void regions (which are actually modeled as extremely dilute gases) result in highly ill-conditioned source iteration equations. Thus this is a very difficult problem to efficiently solve. Note from Fig. 5 that each region represents a coaxial cylinder of uniform composition. A geosynchronous trapped electron source is again incident along the outer periphery. We have performed P_1, P_3, and P_7 calculations using a 35×35 spatial mesh with nonuniform spacing ($\Delta_{\mathrm{Al,Si}}=2.67\times10^{-3}$ cm, $\Delta_W=4.0\times10^{-3}$ cm). Low density nitrogen gas (10^{-7} g/cm^3) was used to simulate the void region in the SP_N calculation, while the Monte Carlo method allows the explicit modeling of a void. For the Monte Carlo calculation we ran 2×10^6 source electron histories. The calculated EDR in the inner aluminum region is given for both the Monte Carlo and SP_N calculations in Table VII together with CPU times.

It can be seen from Table VII that the SP_7 and Monte Carlo values for the EDR in the aluminum are nearly identical, and the CPU time for the SP_7 calculation is about one-sixth that of the Monte Carlo calculation. The SP_N calculations were performed using the black-box multigrid [18] method to solve the source iteration equations. When we attempted to perform the SP_7 calculation using the ICCG solver, the convergence rate was so slow that the calculation had to be terminated. Thus we see that voids can be success-

TABLE VII. Problem five: results.

	EDR (MeV/cm^3 s)	CPU time (s)
SP_1	2.17	225
SP_3	2.20	305
SP_7	2.24	490
MC	$2.25\pm1\%$	3193

fully modeled with a dilute gas, and the BBMG method is far superior to the ICCG method if the problem has highly ill-conditioned source iteration equations. However, one should remember from problem three that the ICCG method can be more efficient than the BBMG method if the source iteration equations are well conditioned.

VIII. CONCLUSIONS

Our results clearly indicate that SP_N method is a valuable alternative to full deterministic and Monte Carlo transport methods for coupled electron-photon space shielding calculations. For the representative problems we considered, the SP_7 approximation appears to be adequate, and gives results that are within 10% of Monte Carlo results. This level of accuracy is considered acceptable for engineering applications. As one might expect from the asymptotic nature of the SP_N equations, increasing the order of the approximation does not always improve the accuracy of the solution. However, neither does it appear to result in a serious increase in error. The SP_N method was clearly very much more efficient than the Monte Carlo method for the problems that were considered, but it is important to recognize that the Monte Carlo method was not biased. As previously discussed, sophisticated variance reduction techniques required for space shielding calculations are not available to the casual user of the CYLTRAN code [11]. Thus we could not investigate the effect of biasing on the efficiency of CYLTRAN. Ideally, we would have preferred to compare computational efficiency with a deterministic transport method, but as previously stated, 2D deterministic transport codes for coupled electron-photon calculations are not yet available to the community. Nonetheless, the lower cost of the SP_N method relative to the S_N method is reasonably well established for neutron transport calculations [15]. One would expect similar relative efficiencies in coupled electron-photon space shielding calculations. Overall, it would appear to us that coupled electron-photon space shielding calculations represent an ideal application for the SP_N method. This is not unexpected from a theoretical viewpoint. The isotropic bath of electrons surrounding the satellite strongly contributes to a solution that is almost locally 1D.

One of the surprising results of our study is that the P_1-DSA and AMG convergence acceleration methods retain their 1D effectiveness in 2D SP_N calculations, even though they can lose their effectiveness in 2D S_N equations. Indeed, these methods can actually become unstable when applied to the S_N equations under the conditions present in the coupled electron-photon transport calculations that we performed.

Finally, we note that we have demonstrated that void regions can be successively modeled with extremely dilute gases. However, the presence of void regions can result in ill-conditioned source iteration equations that require a multigrid diffusion solver such as BBMG [18]. The conjugate-gradient method could certainly be used for such equations if a multigrid preconditioner is used, but nonmultigrid preconditioners such as the incomplete Cholesky method should generally be inadequate for problems with voids. On the other hand, if voids are not present, the ICCG method [17] can be more efficient than the BBMG method.

In the future, we intend to investigate the application of the SP_N method to 3D coupled electron-photon space shielding problems. Furthermore, we intend to investigate the use of 3D adjoint SP_N calculations to bias coupled electron-photon Monte Carlo calculations.

[1] E. M. Gelbard, Westinghouse Report No. WAPD-BT-20, 1960; Westinghouse Report No. WAPD-T-1182, 1961; Westinghouse Report No. WAPD-TM-294, 1962.

[2] E. E. Lewis and W. F. Miller, Jr., *Computational Methods of Neutron Transport* (Wiley, New York, 1984).

[3] E. W. Larsen, J. E. Morel, and J. M. McGhee, in *Proceedings of the American Nuclear Society Topical Meeting, Mathematical Methods and Supercomputing in Nuclear Applications, Karlsruhe, Germany, April 19–23, 1993* (American Nuclear Society, 1993), Vol. 1, pp. 718–729.

[4] E. W. Larsen, J. E. Morel, and J. M. McGhee, Nucl. Sci. Eng. **123**, 328 (1996).

[5] G. C. Pomraning, Ann. Nucl. Energy **20**, 623 (1993).

[6] J. E. Morel and J. M. McGhee, Nucl. Sci. Eng. **120**, 147 (1995).

[7] J. E. Morel, Nucl. Sci. Eng. **82**, 34 (1982).

[8] J. E. Morel and T. A. Manteuffel, Nucl. Sci. Eng. **107**, 330 (1991).

[9] M. L. Adams and T. A. Wareing, Trans. Am. Nucl. Soc. **68A**, 203 (1993).

[10] John A. Josef, Ph.D. thesis, The Pennsylvania State University, 1996, also available as Los Alamos National Laboratory Report LA-UR-97-435, 1997.

[11] J. A. Halbleib, R. P. Kensek, T. A. Mehlhorn, G. D. Valdez, S. M. Seltzer, and M. J. Berger, Sandia National Laboratory Report No. SAND 91-1634, 1992.

[12] K. Przybylski and J. Ligou, Nucl. Sci. Eng. **81**, 92 (1982).

[13] L. J. Lorence, Jr., J. E. Morel, and G. D. Valdez, Sandia National Laboratory Report No. SAND 89-1685, 1989.

[14] J. E. Morel, Nucl. Sci. Eng. **91**, 324 (1985).

[15] J. E. Morel, J. M. McGhee, and E. W. Larsen, Nucl. Sci. Eng. **123**, 319 (1996).

[16] O. C. Zienkiewicz and R. L. Taylor, *The Finite Element Method* (McGraw-Hill Book Company, London, 1994).

[17] Gene H. Golub and Charles F. Van Loan, *Matrix Computations* (John Hopkins University Press, Baltimore, 1983).

[18] J. E. Dendy, Jr., J. Comput. Phys. **48**, 366 (1982).

[19] R. E. Alcouffe, Nucl. Sci. Eng. **64**, 344 (1977).

[20] L. J. Lorence, Jr., J. E. Morel, and E. W. Larsen, Nucl. Sci. Eng. **101**, 341 (1989).

[21] K. D. Lathrop, Nucl. Sci. Eng. **21**, 498 (1963).

[22] L. J. Lorence, Jr., J. E. Morel, and G. D. Valdez, Sandia National Laboratory Report No. SAND 89-1661, 1989.

[23] R. Saqui, T. Jordan, J. Mack, G. Radke, J. Morel, and J. Janni, Air Force Systems Command Weapons Laboratory Report No. WL-TR-90-59, 1991.